Check for updates

Space Weather

RESEARCH ARTICLE
10.1029/2026SW005133

Auroral Effect on Mid-Latitude Ionospheric Disturbances Over Europe During the Extreme Geomagnetic Storm of 10 May 2024

Grzegorz Nykiel[1], Joanna Kanska[2], Hiroatsu Sato[1], Shin-ichiro Oyama[3,4,5], Kazuo Shiokawa[3], and David R. Themens[6]

[1]Institute for Solar-Terrestrial Physics, German Aerospace Center (DLR), Neustrelitz, Germany, [2]Faculty of Civil and Environmental Engineering, Gdansk University of Technology, Gdansk, Poland, [3]Institute for Space-Earth Environmental Research, Nagoya University, Nagoya, Japan, [4]National Institute of Polar Research, Tokyo, Japan, [5]Space Physics and Astronomy Research Unit, University of Oulu, Oulu, Finland, [6]School of Engineering, Space Environment and Radio Engineering (SERENE), University of Birmingham, Birmingham, UK

Key Points:

- GNSS TEC data were used to visualize ionospheric disturbances in the mid-latitude auroral oval above Europe on 10 May 2024
- The enhanced TEC gradients, ROTI, and large-scale disturbances coincided with the optical aurora observations
- The observed TEC disturbances were primarily driven by auroral particle precipitation and the associated electrodynamic processes

Supporting Information:

Supporting Information may be found in the online version of this article.

Correspondence to:

G. Nykiel,
grzegorz.nykiel@dlr.de

Citation:

Nykiel, G., Kanska, J., Sato, H., Oyama, S.-i., Shiokawa, K., & Themens, D. R. (2026). Auroral effect on mid-latitude ionospheric disturbances over Europe during the extreme geomagnetic storm of 10 May 2024. *Space Weather*, *24*, e2026SW005133. https://doi.org/10.1029/2026SW005133

Received 17 APR 2026
Accepted 29 JUL 2026

Author Contributions:

Conceptualization: Grzegorz Nykiel, Hiroatsu Sato
Data curation: Grzegorz Nykiel
Formal analysis: Grzegorz Nykiel, Hiroatsu Sato, David R. Themens
Investigation: Grzegorz Nykiel, Joanna Kanska, Hiroatsu Sato, David R. Themens
Methodology: Grzegorz Nykiel
Resources: Grzegorz Nykiel, Shin-ichiro Oyama, Kazuo Shiokawa
Software: Grzegorz Nykiel, Joanna Kanska
Supervision: Grzegorz Nykiel

© 2026 The Author(s). Space Weather published by Wiley Periodicals LLC on behalf of American Geophysical Union. This is an open access article under the terms of the Creative Commons Attribution License, which permits use, distribution and reproduction in any medium, provided the original work is properly cited.

Abstract Large ionospheric disturbances were observed over Europe during the extreme geomagnetic storm on 10 May 2024. This study analyzes GNSS-derived total electron content (TEC) and all-sky imager data to investigate these disturbances. Pronounced TEC enhancements, irregularities, and strong gradients were confined to the auroral region above the mid-latitudes. These anomalies evolved coherently with the equatorward expansion of the optical aurora. Large-scale TEC disturbances were found to be moving at mid-latitudes with an equatorward velocity of 726 m/s and an amplitude of up to 7 TECU. These characteristics were indicative of the auroral expansion rather than of large-scale traveling ionospheric disturbances (LSTIDs), which exhibited weaker amplitudes near the auroral boundary. This finding contrasts with the interpretation of some previous studies on GNSS observations. This study demonstrates the visualization of the auroral oval at mid-latitudes using TEC and TEC-derived parameters.

Plain Language Summary This article analyzes the extreme geomagnetic storm that occurred from 10 to 13 May 2024. This storm is commonly known as the "Mother's Day Storm" or the "Gannon Storm." It was one of the most intense space weather phenomena in recent decades. The storm reached a maximum level of G5 on the NOAA scale, causing auroras to appear at unusually low latitudes, including southern Europe. Using a combination of data from hundreds of satellite navigation (GNSS) receivers and optical data from an all-sky imager in Germany, we investigated how the storm altered the Earth's ionosphere. Our analysis revealed that significant disturbances in electron density were closely related to the location of the aurora, which expanded toward the equator. Imager data showed that GNSS-based disturbances and gradient indices can identify auroral precipitation in mid-latitudes, causing major ionospheric disturbances. While some GNSS data resemble traveling waves, these waves are actually caused by the same particles that create the aurora. We found large-scale traveling ionospheric disturbances equatorward of the auroral boundary, though they were much smaller in amplitude. Ultimately, our findings underscore the importance of combining satellite data with camera observations to correctly identify these space weather effects and understand their impact.

1. Introduction

The geomagnetic storm that occurred from 10 to 13 May 2024, is commonly known as the Mother's Day Storm or the Gannon Storm. It ranks among the most intense space weather phenomena in recent decades and is categorized as a 1-in-12.5 years storm in terms of intensity and 1-in-41 years in terms of duration (Elvidge & Themens, 2025). A sequence of coronal mass ejections directed toward Earth caused the storm, resulting in prolonged periods of a strong southward interplanetary magnetic field and exceptionally high geomagnetic activity. The storm reached a maximum level of G5 on the NOAA geomagnetic storm scale (Carmo et al., 2024; Elvidge & Themens, 2025). Similar in intensity to the major storms of March 1989 and October–November 2003, the May 2024 event resulted in widespread visibility of the aurora borealis at unusually low latitudes and severe disturbances in the ionosphere and thermosphere.

The storm of May 2024 has been the subject of numerous recent studies due to its intensity and widespread impact on society. These studies have focused on both the storm's geophysical properties and its impact on technological

Validation: Grzegorz Nykiel, Hiroatsu Sato, Shin-ichiro Oyama, Kazuo Shiokawa, David R. Themens
Visualization: Grzegorz Nykiel, Joanna Kanska
Writing – original draft: Grzegorz Nykiel, Joanna Kanska
Writing – review & editing: Grzegorz Nykiel, Hiroatsu Sato, Shin-ichiro Oyama, Kazuo Shiokawa, David R. Themens

systems. Several studies have examined the deterioration of GNSS positioning systems during the storm, documenting increased positioning errors, enhanced phase scintillation, and elevated total electron content (TEC) gradients in many regions (Park et al., 2025; Themens et al., 2024; Yang & Morton, 2025; Younas et al., 2025). Other studies have examined the storm impact on ground-based magnetometer observations (De Michelis & Consolini, 2025), satellite drag and thermosphere density increase (Parker & Linares, 2024), aviation surveillance systems (Schmölter & Berdermann, 2025), and power grid disturbances (Caraballo & Bettucci, 2025; Mota et al., 2025). These studies underscore the far-reaching consequences of extreme geomagnetic storms on the dynamics of geomagnetic space and technological infrastructure.

Many publications document the occurrence of storm ionospheric disturbances during the May 2024 event. These publications highlight the disturbances' global reach and marked regional variability. Berényi et al. (2025) document the equatorward expansion of auroral and subauroral ionospheric conditions over Europe. These conditions include strong TEC gradients, increased westward ion drift and structured electron density perturbations that correspond to large-amplitude traveling ionospheric disturbances (TIDs) in the mid-latitude ionosphere. Tang et al. (2025) showed large-scale TIDs propagating from the auroral zone over Europe and North America. They argued that these TIDs have horizontal wavelengths of a few thousand kilometers, periods of tens of minutes, and their phase fronts and propagation directions are consistent with atmospheric gravity waves launched by high-latitude energy input. Paul et al. (2025) focus on the European sector, reporting pronounced medium- and large-scale TIDs in GNSS-derived station-based TEC. They also report a strong negative storm phase and marked longitudinal and latitudinal variability of the disturbance pattern. Cheng and Morton (2025) further adds an event-wide perspective by quantifying the timing, amplitude, and propagation characteristics of storm-time TEC perturbations. It relates these characteristics to solar wind drivers and magnetospheric forcing.

Despite the growing number of studies devoted to the May 2024 geomagnetic storm, several aspects of the ionospheric response over Europe remain inadequately investigated. This event was unique in that auroral emissions were observed in regions far from their typical locations and overlapping areas that are usually classified as mid-latitudes (Grandin et al., 2024). GNSS-based TEC analyses have revealed the widespread occurrence of TIDs during the storm; however, fewer studies have examined their spatial structure and evolution in relation to simultaneous optical observations of auroral activity at mid-latitudes.

In this study, we analyze the ionospheric response over Europe during the geomagnetic storm that occurred on 10 May 2024. We use observations from several hundred GNSS receivers, combined with the All-sky Imager (ASI) data located at Zugspitze, Germany. All-sky imaging provides valuable context for interpreting ionospheric disturbances obtained from GNSS by offering information on the morphology of the aurora and its motion. Through a joint analysis of TEC, TEC gradients, and the Rate Of TEC Index (ROTI), together with aurora observations, we investigate how ionospheric disturbances evolved in space and time as the auroral oval expanded toward the equator. Our analysis focuses on identifying and characterizing large-scale disturbances and assessing their relationship to auroral dynamics observed at mid-latitudes. This approach provides new insights into the behavior of the ionosphere over Europe during storms and underscores the importance of multi-instrument observations in understanding extreme space weather phenomena.

2. Data and Methodology

2.1. All-Sky Imager

To observe aurora we used the OI (630.0 nm) oxygen emission captured by ASI located on Zugspitze, Germany (47.42°N, 10.98°E). This camera (Z002) is a part of the Optical Mesosphere Thermosphere Imagers (OMTI) system (Shiokawa et al., 2009). OI emission comes from the bottomside of the ionospheric F-layer at 200–300 km and are excited by interactions of oxygen ion (O^+) and molecular oxygen (O_2) (Ogawa et al., 2009; Shiokawa et al., 2003; Sobral et al., 1993). The intensity of the OI 630-nm airglow is a sensitive indicator of the variations in ion density, since the oxygen ion density is basically equal to the electron density at these altitudes (Shiokawa et al., 2009). The emission can also be enhanced by electron precipitation through direct excitation of atomic oxygen (Meier et al., 1989).

The OI 630-nm images with a resolution of 1,408 × 1,408 pixels were taken every 5.5 min with an exposure time of 165 s by a CMOS detector (ZWO ASI294MM Pro). Spatial calibration of the fish-eye lens images was performed using stars as reference points, according to the methodology presented by Garcia et al. (1997). Images

15427390, 2026, 8, Downloaded from https://agupubs.onlinelibrary.wiley.com/doi/10.1029/2026SW005133 by Dtsch Zentrum F. Luft-U. Raum Fahrt In D. Helmholtz Gemein., Wiley Online Library on [06/10/2026]. See the Terms and Conditions (https://onlinelibrary.wiley.com/terms-and-conditions) on Wiley Online Library for rules of use; OA articles are governed by the applicable Creative Commons License

15427390, 2026, 8, Downloaded from https://agupubs.onlinelibrary.wiley.com/doi/10.1029/2026SW005133 by Dtsch Zentrum F. Luft-U. Raum Fahrt In D. Helmholtz Gemein., Wiley Online Library on [06/10/2026]. See the Terms and Conditions (https://onlinelibrary.wiley.com/terms-and-conditions) on Wiley Online Library for rules of use; OA articles are governed by the applicable Creative Commons License

obtained during 22:02–23:48 UT on May 10 were mapped onto a horizontal plane in geographic coordinates by assuming an emission altitude of 250 km. The field of view (FOV) has a diameter of about 1,100 km at 250 km altitude for a zenith angle of 65° (Ogawa et al., 2009). Next, we visually determined the equatorward boundary of the aurora by identifying points at which the intensity changed and began to decrease. Each image was processed separately. Despite the assumptions used in previous studies, the location of the aurora determined here may be uncertain. This uncertainty results from the adopted emission height. For 630 nm, the peak emission height is 250 km; however, the measurement range is 200–300 km (Shiokawa et al., 2003). Additionally, auroral emission has a different vertical distribution that cannot be characterized with data from one camera. However, different emission levels do not significantly affect the location of the equatorward border of the aurora. In our case, the uncertainty is approximately 0.5°. Furthermore, visual inspection of the equatorward boundary is ambiguous due to the faint latitudinal gradient of emission intensity. In this case, we estimate the error to be up to 0.5°.

2.2. GNSS

In our study we used data from about 400 GNSS stations belonging to the EUREF Permanent GNSS Network (EPN). GPS and Galileo observations, with 30-s interval, were used for computation of various ionospheric parameters which allow for the exploration of temporal and spatial characteristics of the ionospheric response to the geomagnetic storm. Based on the phase observation, for each satellite-receiver path, we estimated absolute slant TEC using the approach described by Ma and Maruyama (2003). Satellite differential code biases were taken from Institute of Geodesy and Geophysics (IGG) of the Chinese Academy of Sciences (CAS) in Wuhan (Wang et al., 2015). Conversion to the vertical TEC was done by applying the thin layer mapping function (Schaer, 1999). To be consistent with all-sky imager data, we applied an ionospheric single layer model with an altitude of 250 km. While storm-time uplift of the F region may introduce spatial uncertainty in ionospheric pierce point locations, this assumption does not affect the conclusions regarding the relative spatial confinement of the observed disturbances.

In addition to absolute TEC values, we also determined TEC anomalies (dTEC) which can represents the existence of TIDs (Borries et al., 2009; Vadas et al., 2025). We obtained these anomalies by filtering the TEC time series for each receiver-satellite pair. In our case, we used a 15–60 min moving average filter. This approach is effective and enables the successful detection of LSTIDs during geomagnetic storms (Nykiel, Ferreira, et al., 2024).

To investigate spatial gradients we applied the methodology proposed by Jakowski and Hoque (2019). For each pair of the receivers, a dipole is created between two ionospheric piercing points (IPPs) i and j of the same satellite s. For such a dipole, the TEC gradient is computed as:

$$\nabla \mathrm{TEC}_{ij}^{s} = \frac{\mathrm{TEC}_{i}^{s} - \mathrm{TEC}_{j}^{s}}{d_{ij}} \tag{1}$$

where d_{ij} is a dipole range representing distance between both points. We calculated gradients only between points with a distance between 50 and 500 km.

Such estimated gradients can be split into northward (meridional, $\nabla \mathrm{TEC}y_{ij}^{s}$) and eastward (zonal, $\nabla \mathrm{TEC}x_{ij}^{s}$) components:

$$\nabla \mathrm{TEC}y_{ij}^{s} = \nabla \mathrm{TEC}_{ij}^{s} \cdot \sin \delta \tag{2}$$

$$\nabla \mathrm{TEC}x_{ij}^{s} = \nabla \mathrm{TEC}_{ij}^{s} \cdot \cos \delta \tag{3}$$

where δ is the angle that defines the azimuth of the TEC gradient.

Using gradients determined from multiple stations in a specific region, one can calculate the Gradient Ionosphere Index (GIX) (Jakowski & Hoque, 2019), which describes the characteristics of the spatial gradients of ionospheric disturbances. The GIX can detect large-scale ionization fronts and provide information on their amplitude and direction (Nykiel, Cahuasquí, et al., 2024). The GIX is calculated as the square root of the sum of the squares of the average value of all zonal and meridional gradients.

$$\mathrm{GIX}(t) = \sqrt{< \nabla\mathrm{TEC}x(t)^2 > + < \nabla\mathrm{TEC}y(t)^2 >} \quad (4)$$

where <> means average of all values within specific region. In our study, we define it between 10°W–30°E and 45°N–75°N. $< \nabla\mathrm{TEC}x(t)^2 >$ and $< \nabla\mathrm{TEC}y(t)^2 >$ are named as zonal and meridional GIX: GIX_x and GIX_y, respectively.

To estimate the level of the ionospheric irregularities, we also used the Rate of TEC Index (ROTI) (Pi et al., 1997) which is calculated as a standard deviation of rate of change of TEC over time. In our study, we calculated ROTI by aggregating measurements over a period of 5-min. Thus, it represents a mixed effect of ionospheric perturbations—temporal changes and small-scale spatial irregularities. Here, ROTI is used qualitatively as an indicator of high ionospheric irregularities caused by particle precipitation and rapidly evolving small spatial gradients, not strictly as a scintillation metric.

3. Results and Discussion

Figure 1 shows IMF Bz and solar wind speed, as well as the AE, Kp, and GIX indices, during the geomagnetic storm period. The IMF Bz component obtained from the ACE2 instrument is displayed in Figure 1a. A notable increase in Bz is evident at approximately 16:55 UT, as evidenced by the available data. Concurrently, a significant increase in solar wind speed was observed, ranging from approximately 470 to 665 km/s, which was associated with the passage of the CME (Figure 1b). Consequently, from approximately 17:07 UT, a clear increase and variation in the AE index became evident (Figure 1c). A high Kp value of 7.7 was also documented for this interval. As the geomagnetic storm developed, the Kp index reached a value of 9. As early as 17:14 UT, Bz reached a temporary value of −40 nT. The first longer period with low Bz values occurred from approximately 18:03 to 18:41 UT and from 20:00 to 21:30 UT. Such periods repeated until 15:00 UT on May 11. The lowest Bz value was −58 nT around 23:48 UT. Throughout the period of significant Bz variations, the AE index exhibited high values, surpassing 2,500 at approximately 19:18 UT and reaching over 4,100 at 19:48 UT (Figure 1c). The high AE values persisted until the end of May 12. A high AE value indicates high global geomagnetic activity in the auroral zone, driven by strong auroral electric currents—that is, large differences between eastward and westward currents. All of this suggests the occurrence of the aurora. During strong geomagnetic storms, aurora oval can expand toward equator. This has been confirmed by numerous reports. For example, Grandin et al. (2024) indicated that the aurora on May 10 was observed in France and even southern Spain based on citizen science observations and ionosonde observations measured auroral E-Region precipitation in Belgium in Europe and, briefly, in Florida in the United States (Themens et al., 2024).

3.1. Aurora Optical Observations

The mid-latitude red aurora was visible in the sequence of 630 nm images registered by the ASI located on Zugspitze, Germany (Figure 2). The aurora approached from the northern horizon at 22:07:30 UT on May 10 and continued to expand to a latitude of 45°N geographic latitude for the next half an hour, after which it began to weaken. The green aurora was observed at 557.7 nm emission at the same time (see Figure S1 in Supporting Information S1). This suggests that both emissions originated in the same magnetospheric region and that the energy of the auroral electrons spread over a wide range, resulting in emissions at different altitudes. From 22 UT, a stable auroral red (SAR) arc was visible in the 630 nm images and began to fade at around 23:30 UT. Thermal heat fluxes are considered as a source of SARs emission (Inaba et al., 2021; Nishimura et al., 2022; Upadhyay & Pallamraju, 2024), but Mendillo et al. (2016) found evidence that the low-energy electron precipitation can also be the SAR arc modulating mechanism. A weaker emission was also observed, which was visible in the images throughout the night, from 22:02:00 UT on May 10 to 02:18:30 UT on May 11. During the aurora, the emission expanded to latitude of 43°N, then receded and remained stable at 45°N until the end of the observation period.

3.2. GNSS TEC-Derived Parameters

Figure 1e illustrates the total GIX index alongside its zonal (GIX_X) and meridional (GIX_Y) components. These indices were determined for the 45°N–75°N area and represent the average gradient value over distances ranging from 50 to 500 km. Around 20:15 UT, the GIX_Y value began showing positive values, indicating the presence of northward gradients. The maximum GIX_Y value occurred around 22:17 UT, amounting to 16 mTECU/km. As the

15427390, 2026, 8, Downloaded from https://agupubs.onlinelibrary.wiley.com/doi/10.1029/2026SW005133 by Dtsch Zentrum F. Luft-U. Raum Fahrt In D. Helmholtz Gemein., Wiley Online Library on [06/10/2026]. See the Terms and Conditions (https://onlinelibrary.wiley.com/terms-and-conditions) on Wiley Online Library for rules of use; OA articles are governed by the applicable Creative Commons License

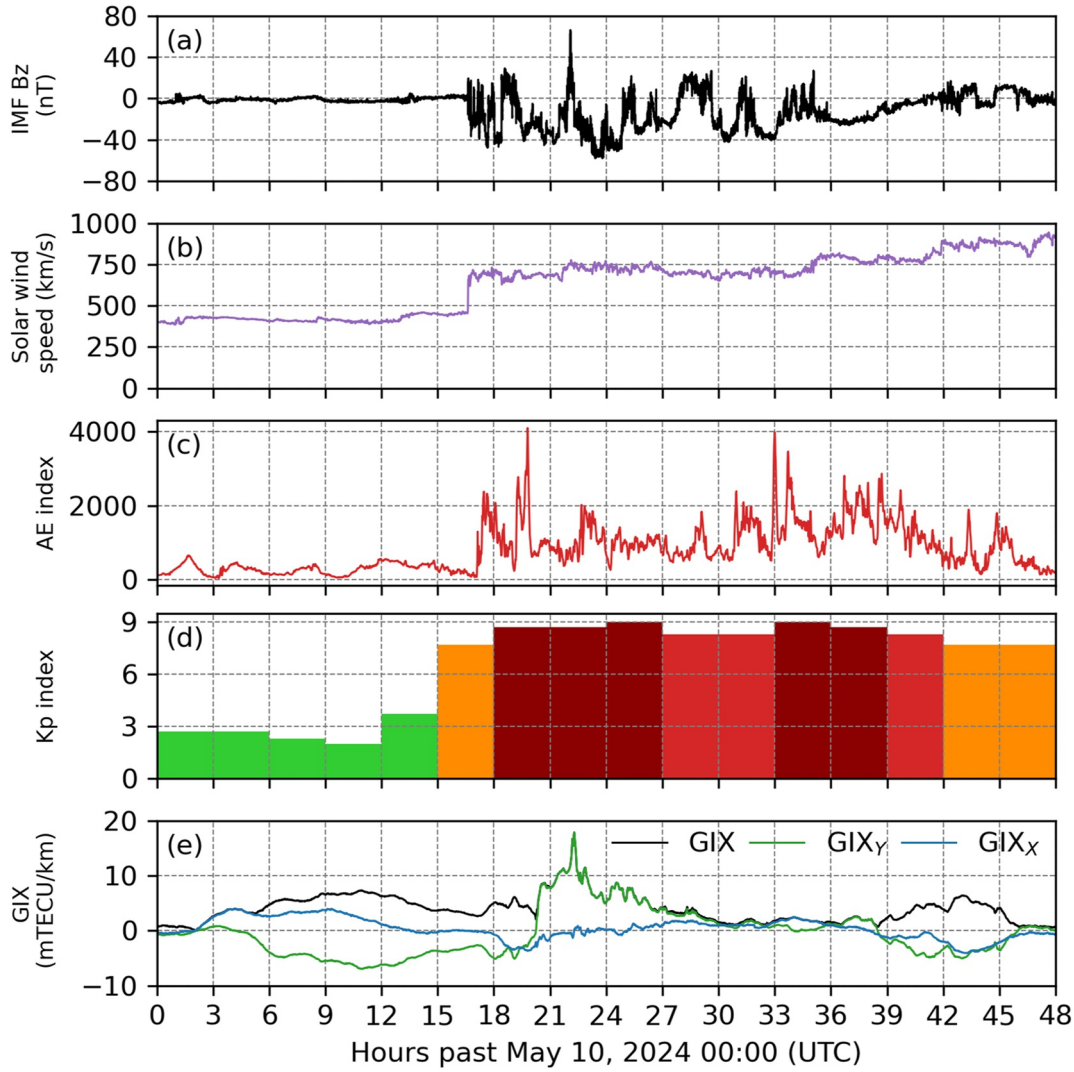

Figure 1. Selected parameters for days 10–11 May 2024: (a) the Interplanetary Magnetic Field (IMF) component Bz (Geocentric Solar Ecliptic (GSE) frame); (b) solar wind speed; (c) Auroral Electrojet index (AE); (d) Kp index; (e) total Gradient Ionospheric indeX (GIX) and zonal (GIX$_X$) and meridional components (GIX$_Y$).

total GIX takes on the same values, the graph shows that there were no clear zonal gradients at that time. The large northward gradient may be explained by an increase in TEC at higher latitudes caused by auroral particle precipitation. Figure 3 confirms this, showing the zonal distribution of TEC, ROTI and dTEC, as well as TEC gradients, for the three selected epochs for which ASI data was available. The dashed line indicates the southern boundary of the auroral oval and the dashed-dotted line indicates the SAR boundary. Figure 3a clearly shows high TEC values corresponding to the location of the auroral oval. These values reached approximately 45 TECU at 22:13 UT, which was nearly 30 TECU higher than the previous day (Figure 3b). Later in the storm's duration over North America, Foster et al. (2024) observed a similar effect, where intense red auroras occurred at the equatorward edge of increased TEC values. Higher TEC values in the auroral region are also evident in the meridional gradients (Figure 3c), with gradient values reaching almost 40 mTECU/km in some places. Red values represent positive gradients, meaning that TEC values increase toward the north. Based on these results, we conclude that the transition between northern and southern gradients (where the gradient values equal zero) coincides with the SAR boundary, as obtained from ASI. The gradient maps also clearly show large negative gradient values around 55°N, which may indicate the northern border of the aurora.

15427390, 2026, 8, Downloaded from https://agupubs.onlinelibrary.wiley.com/doi/10.1029/2026SW005133 by Dtsch Zentrum F. Luft-U. Raum Fahrt In D. Helmholtz Gemein., Wiley Online Library on [06/10/2026]. See the Terms and Conditions (https://onlinelibrary.wiley.com/terms-and-conditions) on Wiley Online Library for rules of use; OA articles are governed by the applicable Creative Commons License

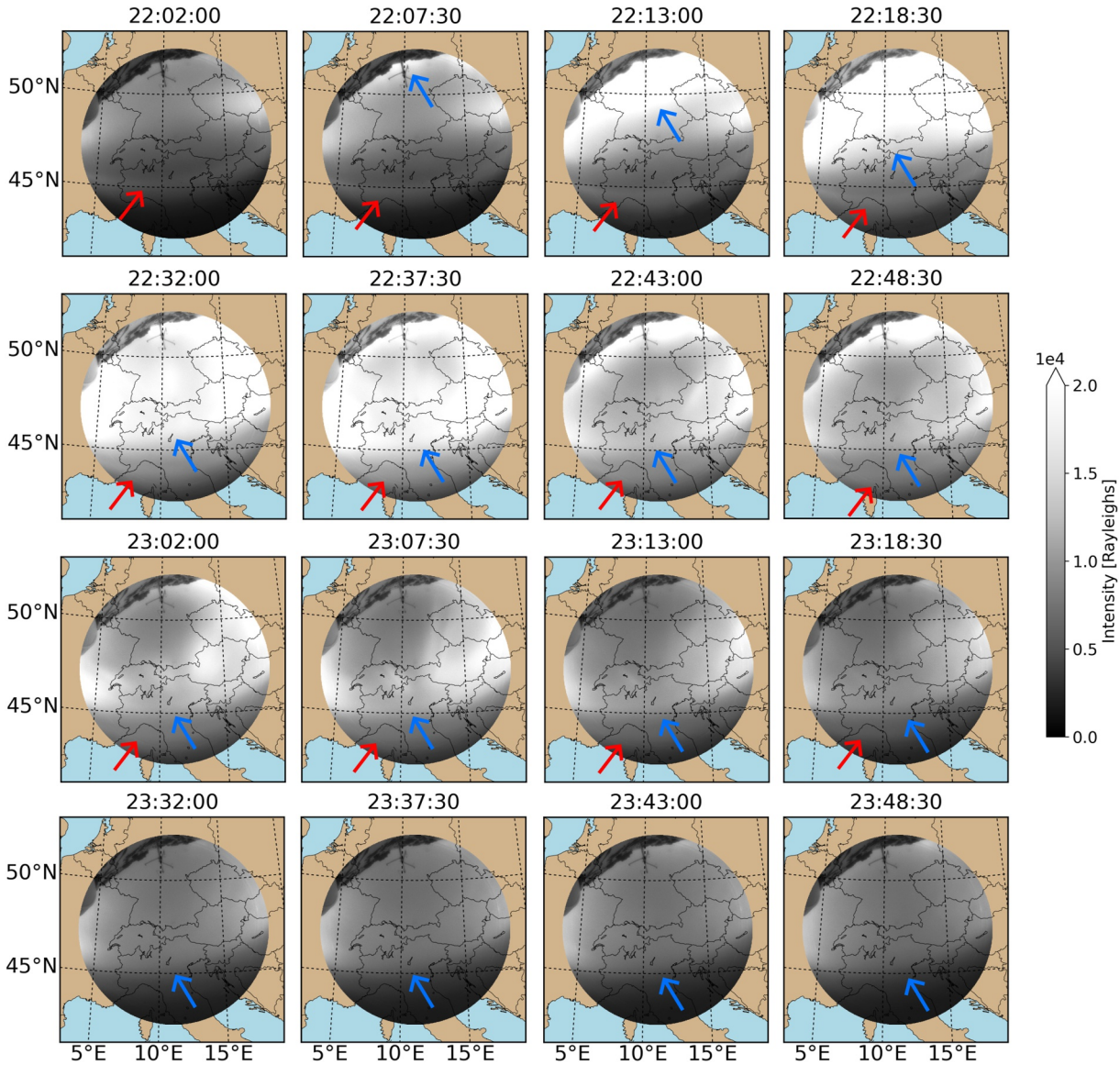

Figure 2. Time series of 630-nm all-sky images obtained at 22:02–23:48:30 UT on 10 May 2024, on Zugspitze (47.42°N, 10.98°E), Germany. The images are oriented to the north. The red arrows show the stable auroral red (SAR) arc, and the blue arrows show the expanding aurora.

Sudden increases in TEC in mid-latitudes can be associated with strong particle precipitation. Previous studies (Astafyeva et al., 2022; Makarevich et al., 2021) suggest that ROTI can serve as proxy for particle precipitation. To confirm this statement, we used the Special Sensor Ultraviolet Spectrographic Imager (SSUSI), which was flown aboard Defense Meteorological Satellite Program (DMSP) satellites, to check for a coincidence between particle precipitation and increased ROTI values. Unfortunately, the satellite's observation times were inconsistent with the optical observations. However, for the earlier hours of 18:45 and 20:25 UT, we compared the electron energy flux derived from the satellite F17 with ROTI (Figure 4). For both of these periods, there are clearly increased ROTI values further poleward of 55°N. Although the SSUSI DMSP data range does not precisely overlap, it is consistent with increased ROTI values. This implies a distinct auroral correspondence of ROTI.

Figure 3d shows 5-min ROTI, high values (even exceeding 7 TECU/min) were observed in the area of increased TEC. Strong particle precipitation occurred in this region, causing a transient increase in TEC through the direct ionization of the neutral atmosphere. At the same time and in the same area, we observed increased TEC anomalies with an amplitude of up to 10 TECU (Figure 3e). However, these perturbations do not exhibit the

15427390, 2026, 8, Downloaded from https://agupubs.onlinelibrary.wiley.com/doi/10.1029/2026SW005133 by Dtsch Zentrum F. Luft-U. Raum Fahrt In D. Helmholtz Gemein., Wiley Online Library on [06/10/2026]. See the Terms and Conditions (https://onlinelibrary.wiley.com/terms-and-conditions) on Wiley Online Library for rules of use; OA articles are governed by the applicable Creative Commons License

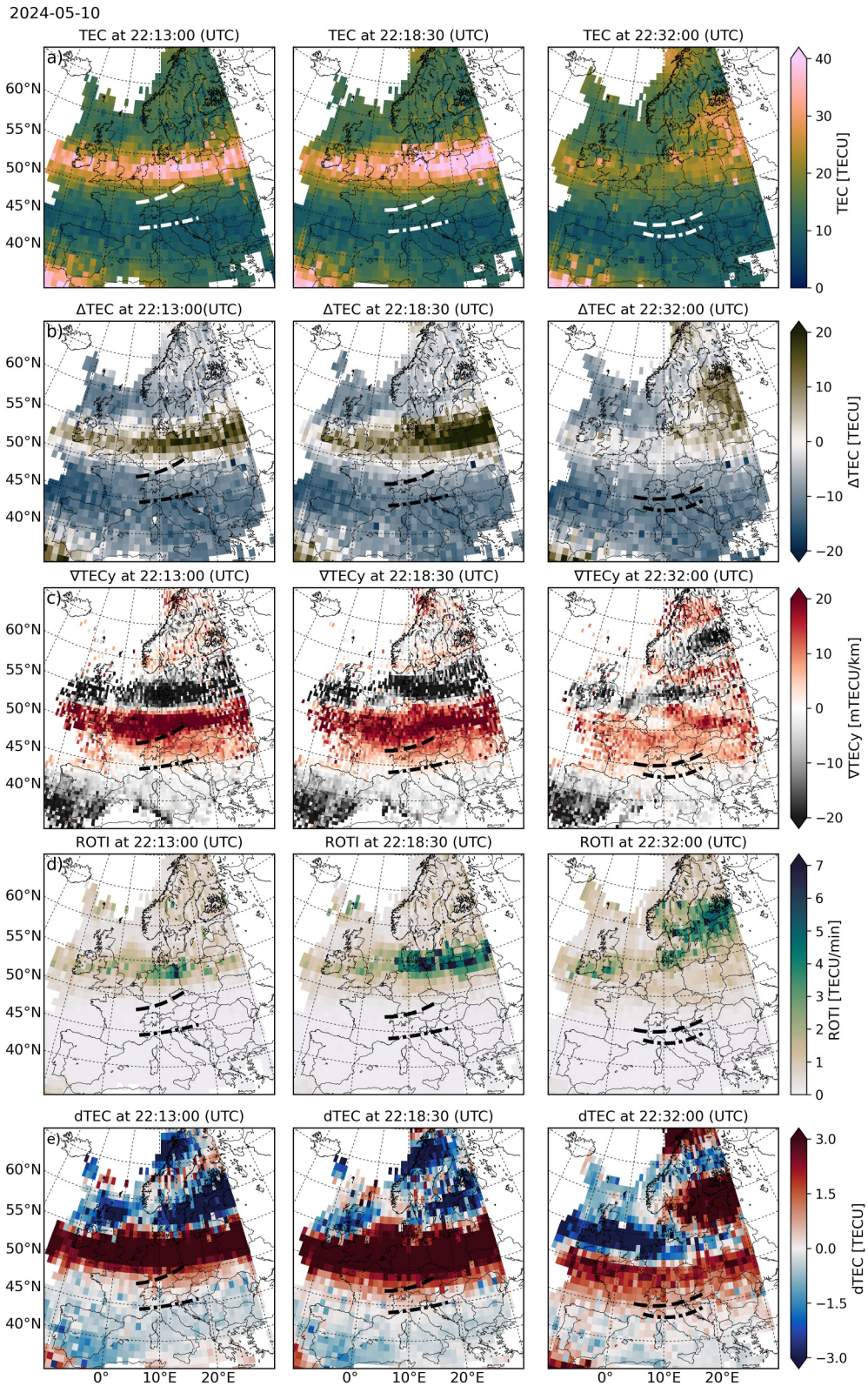

Figure 3.

15427390, 2026, 8, Downloaded from https://agupubs.onlinelibrary.wiley.com/doi/10.1029/2026SW005133 by Dtsch Zentrum F. Luft-U. Raum Fahrt In D. Helmholtz Gemein., Wiley Online Library on [06/10/2026]. See the Terms and Conditions (https://onlinelibrary.wiley.com/terms-and-conditions) on Wiley Online Library for rules of use; OA articles are governed by the applicable Creative Commons License

15427390, 2026, 8, Downloaded from https://agupubs.onlinelibrary.wiley.com/doi/10.1029/2026SW005133 by Dtsch Zentrum F. Luft-U. Raum Fahrt In D. Helmholtz Gemein., Wiley Online Library on [06/10/2026]. See the Terms and Conditions (https://onlinelibrary.wiley.com/terms-and-conditions) on Wiley Online Library for rules of use; OA articles are governed by the applicable Creative Commons License

characteristics of large-scale TIDs that propagate into the mid-latitudes. None of the parameters exceed the aurora boundary obtained from ASI. Figure 3a shows a decrease in TEC around 50°N and 10°E at 22:32 UT. One possible cause of this decrease may be a reduction in the intensity of particle precipitation, as represented by ROTI. At 22:13 and 22:18:30 UT, values in this region exceeded 7 TECU/min. However, by 22:32 UT, it decreased to no more than 4 TECU/min. Furthermore, the auroral zone is heated by strong particle precipitation and Joule heating, which causes upwelling and rapid recombination of NO^+/O_2^+. This results in a rapid decrease in TEC. Although this is not clearly visible in the figure, examining the gradient values reveals that the TEC values within the auroral oval remain consistently higher than those poleward and equatorward of it.

Figure 5 presents how the ionospheric parameters obtained from GNSS changed over time along the 11°E meridian, where the ASI is located. Figure 5a shows the TEC distribution. There is a clear increase in TEC at higher latitudes, which began around 18:30 UT and propagated southward. TEC values at that time ranged from 25 TECU to 45 TECU. Compared to the previous day's data, the average increase in TEC values was about 5 TECU (Figure 5b), which is approximately 23% of the previous day's TEC values. Due to the nighttime hours and the progression of composition-related plasma depletion (Themens et al., 2024), a systematic decrease in TEC is clearly visible in the mid-latitudes. This mid-latitude ionospheric trough is associated with large horizontal gradients in the norther direction (Figure 5c). Those gradients reached up to 34 mTECU/km at 20.30 UT and 26 mTECU/km at around 22:00 UT when sudden increased TEC occurred. By comparing the distribution of gradients to the extent of the auroral oval (the dashed line), and especially to location of SAR (the dashdotted line), as seen by the ASI, we can conclude that the auroral boundary between 22:00 and 00:00 UT coincides with the transition of the northern and southern gradients. Using this method, we can extrapolate to previous epochs and determine the extent of the aurora using gradient distributions (the dotted line). Additionally, it follows that the expansion of the auroral oval was accompanied by the southward propagation of the mid-latitude ionospheric trough. As with the results shown in Figure 3, the same is true in this case (5d). Strong particle precipitation occurred in the area where an increase in TEC was observed, consistent with the interpretation of Themens et al. (2024), who, using hemispheric TEC imagery, associate these TEC enhancements to auroral precipitation, inferred through the observation of substorm expansions throughout the storm. At that time, ROTI values ranged from 0.5 to 4.5 TECU/min and propagated southward in tandem with TEC changes. The occurrence of particle precipitation in this area caused an aurora whose extent coincided with ROTI, TEC, and gradient increases. Figure 5 clearly shows this, as it marks the southern boundary of the aurora, reconstructed from the ASI, with a dashed line.

3.3. Large-Scale Disturbances

We used dTEC data to assess the occurrence and characteristics of the TIDs during this period at mid latitudes and check their connection to the aurora. Figure 5e shows TEC anomalies obtained using a 15–60-min bandpass filter, which can be used to identify the structures and characteristics of TIDs. North of 50°N, there are many positive and negative dTECs with high amplitudes. The largest of these, marked as I, occurred around 20:30 UT. However, their shape and amplitude (up to 12 TECU) differ from the typical values of LSTIDs, as described in Ding et al. (2008), or from those observed during previous major events over Europe (Nykiel, Ferreira, et al., 2024). Furthermore, in most regions where large dTEC anomalies occur, there is also a significant increase in ROTI, suggesting strong particle precipitation. Since these areas are poleward of the boundary defined by positive TEC gradient values (Figure 5c), we conclude that these dTEC anomalies occur within the auroral region. We conclude that north of 50°N, there are no visible dTEC structures after 17:00 UT that could be interpreted as LSTIDs.

After 22:00 UT, area II exhibits a significant positive dTEC anomaly of up to 7 TECU. In this case, however, this area coincides with the location of a strong positive ROTI. The area of the positive dTEC anomaly moves southward but does not exceed the aurora boundary, which is marked by the black dashed line. The velocity of the observed structure was determined using linear regression. The slope of the resulting line represents the velocity.

Figure 3. Maps showing the spatial distribution of ionospheric parameters derived from GNSS observations: (a) total electron content (TEC); (b) TEC differences (ΔTEC) compared to previous day; (c) meridional TEC gradients (∇TEC_y); (d) Rate Of TEC Index (ROTI); (e) TEC anomalies (dTEC); Results presented for the three selected epochs: 22:13:00 (left), 22:18:30 (middle) and 22:32:00 UT (right) on 10 May 2024. The results are binned into a regular grid of 1° × 1° (0.25° × 0.25° for ∇TEC_y). The dashed line represents the boundary of the auroral oval, and the dashdotted line denotes the boundary of the stable auroral red (SAR), which was obtained from an all-sky imager located on Zugspitze, Germany.

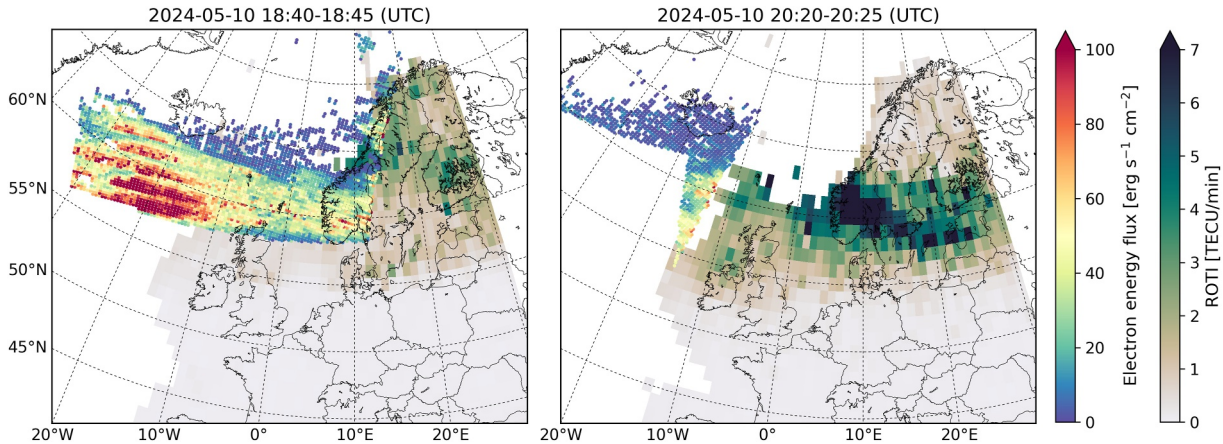

Figure 4. Electron energy flux derived from the SSUSI DMSP (satellite F17) on the background of the 5-min Rate Of TEC Index (ROTI) derived from GNSS observations.

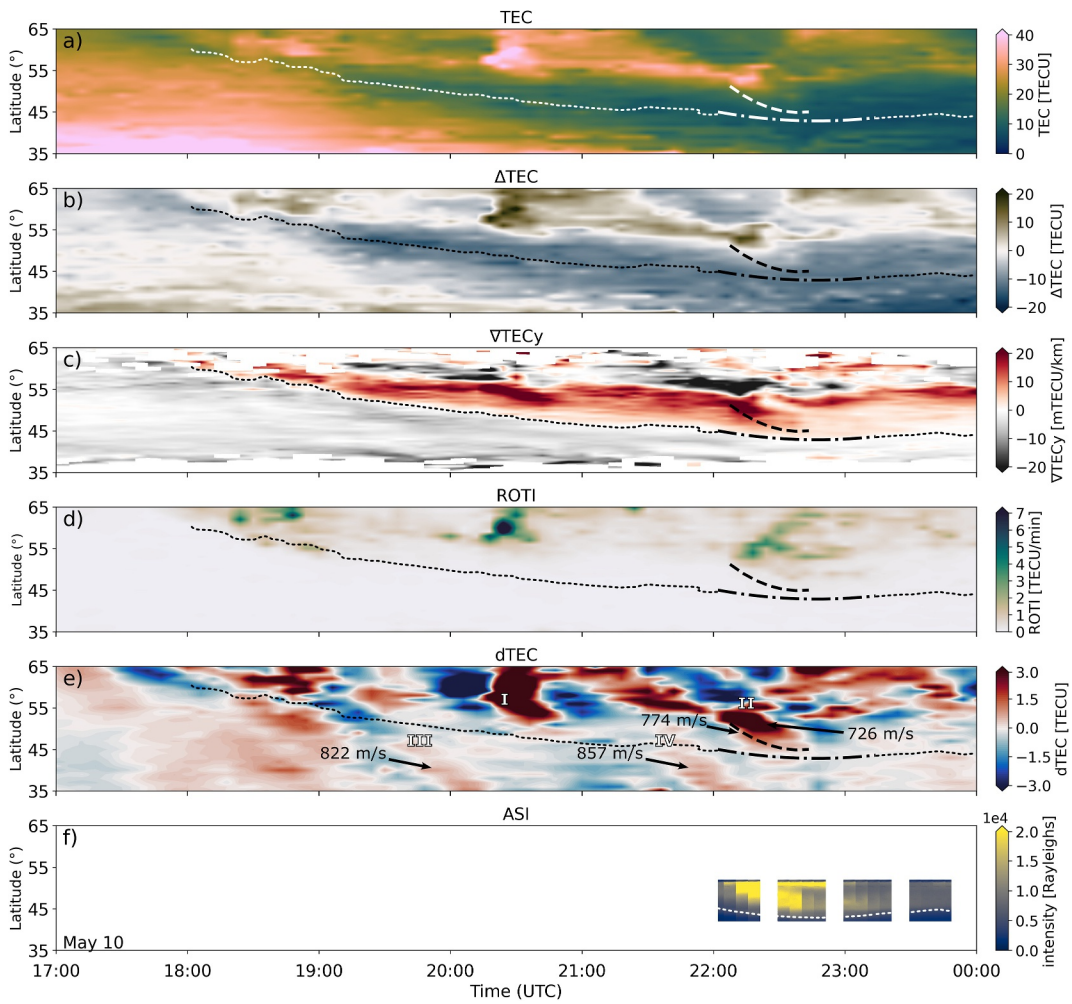

Figure 5. Latitude time-plots along the 11°E: (a) total electron content (TEC); (b) TEC differences (ΔTEC) compared to previous day; (c) meridional TEC gradients (∇TEC*y*); (d) Rate Of TEC Index (ROTI); (e) TEC anomalies (dTEC); (f) intensity derived from all-sky imager (ASI) at a 630.0 nm wavelength. The dashed line represents the boundary of the auroral oval, and the dashdotted line denotes the boundary of the stable auroral red (SAR), which was obtained from an all-sky imager located on Zugspitze, Germany. The dotted line indicates the location at which the ∇TEC*y* change direction.

15427390, 2026, 8, Downloaded from https://agupubs.onlinelibrary.wiley.com/doi/10.1029/2026SW005133 by Dtsch Zentrum F. Luft-U. Raum Fahrt In D. Helmholtz Gemein., Wiley Online Library on [06/10/2026]. See the Terms and Conditions (https://onlinelibrary.wiley.com/terms-and-conditions) on Wiley Online Library for rules of use; OA articles are governed by the applicable Creative Commons License

15427390, 2026, 8, Downloaded from https://agupubs.onlinelibrary.wiley.com/doi/10.1029/2026SW005133 by Dtsch Zentrum F. Luft-U. Raum Fahrt In D. Helmholtz Gemein., Wiley Online Library on [06/10/2026]. See the Terms and Conditions (https://onlinelibrary.wiley.com/terms-and-conditions) on Wiley Online Library for rules of use; OA articles are governed by the applicable Creative Commons License

In this case, it was 726 m/s. This value is similar to that obtained directly from GNSS measurements for two stations located near the 11°E meridian. Considering the baseline between the GOET (51.50°N, 9.95°E) and PFA3 (47.53°N, 9.78°E) stations, we found a velocity of 735 m/s during the positive anomalies around 22:00 UT using dTEC for each satellite (not shown). Then, using data from the ASI, we determined the velocity of the aurora's southern expansion. By comparing the intensity along the 11°E meridian in the images, we obtained a result of 774 m/s, which is very close to values determined from the dTEC keogram and individual GNSS stations. This motion of the observed TEC disturbances reflects the displacement of the auroral forcing region rather than the propagation of a freely traveling wave. Based on our results, we conclude that, contrary to what has been described in other studies (Paul et al., 2025; Tang et al., 2025), the dominant TEC disturbances on May 10 were directly controlled by auroral forcing rather than classical freely propagating LSTIDs.

Our results show the subsequent propagating weak LSTIDs structure generated by the auroral expansion (III and IV). The first one occurred at around 20:00 UT and propagated southward from approximately 47.5°N with a velocity about 822 m/s. The second one appeared between 21:45 and 22:00 UT equatorward of the auroral oval (around 50°N) and propagates equatorward at a velocity of approximately 857 m/s. This corresponds well with a weak substorm that occurs at that time, but its magnitude is much weaker (it does not exceed 1 TECU) than the dTEC observed during auroral precipitation. The occurrence of LSTID in this time was mentioned by Berényi et al. (2025) based on ionosonde data from Hungary and Italy. These TIDs are most likely true TIDs rather than a suppressed continuation of the phenomenon within the auroral oval resulting from auroral precipitation, as we have demonstrated. These weak TIDs are probably generated by Joule heating resulting from pulsations in auroral activity/currents. They propagate equatorward, creating the impression of a continuous TEC structure spreading from higher latitudes. In reality, these are two distinct processes (Prikryl et al., 2022). Furthermore, these LSTIDs do not cause any ROTI or VTEC fluctuations. These strong ROTI/VTEC enhancements are only associated with auroral particle precipitation.

Intense auroral energy input can generate atmospheric gravity waves that propagate equatorward, manifesting as storm-time ionospheric disturbances (Nykiel, Ferreira, et al., 2024). In this case, however, the dominant TEC perturbations remained confined to the auroral region, with no clear evidence of sustained, freely propagating disturbances extending to lower latitudes. This suggests that even if gravity waves were generated, they did not play a significant role in the mid-latitude TEC response during this period. Instead, the observations suggest that auroral particle precipitation and the associated electrodynamic processes were the primary drivers of the observed TEC structures.

4. Conclusions

Dense GNSS observations combined with simultaneous all-sky imager (ASI) data were used to study the ionosphere's response over Europe during the extreme geomagnetic storm on 10 May 2024. This was one of the first times we were able to comprehensively monitor the equatorward expansion of the auroral oval into Europe's mid-latitudes and investigate the relationship between auroral dynamics and ionospheric disturbances.

The results revealed significant enhancements in total electron content (TEC), steep TEC gradients, an increased Rate of TEC Index (ROTI), and large-scale TEC anomalies confined to regions impacted by auroral precipitation and stable auroral red (SAR) arcs. These disturbances' spatial extent and temporal evolution closely followed the movement of the auroral boundary observed in optical data. Southward-moving TEC disturbances were detected but did not propagate beyond the auroral region; their apparent velocities matched the motion of the aurora itself. These findings suggest that the observed ionospheric disturbances were primarily driven by local auroral forcing and associated electrodynamic processes rather than freely propagating, large-scale traveling ionospheric disturbances (LSTIDs). A few isolated, low-intensity LSTIDs likely related to Joule heating were identified but contributed minimally to overall TEC variability.

This study demonstrates that auroral activity can strongly restructure the mid-latitude ionosphere during extreme geomagnetic storms, producing TEC signatures that resemble LSTIDs. Imager data provides evidence that ROTI and gradient indices effectively identify the presence or absence of auroral activity/precipitation in mid-latitudes during severe storms. Therefore, users of GNSS TEC data should take the ROTI index or other gradient indices into account when interpreting GNSS TEC anomalies during such events.

Conflict of Interest

The authors declare no conflicts of interest relevant to this study.

Availability Statement

RINEX files from GNSS stations belonging to the EUREF Permanent GNSS Network (EPN) can be downloaded from: https://epncb.oma.be/_networkdata/data_access/. Digital data in CDF format from cameras belonging to Optical Mesosphere Thermosphere Imagers can be obtained from: https://ergsc.isee.nagoya-u.ac.jp/data/ergsc/ground/camera/. The DMSP SSUSI data were obtained from the NASA Coordinated Data Analysis Web (CDAWeb): https://cdaweb.gsfc.nasa.gov.

Acknowledgments
We thank the EUREF Permanent GNSS Network (EPN) and EarthScope Consortium for providing GNSS RINEX files from permanent stations. The GNSS data were processed at the Academic Computer Centre in Gdansk, Poland. We also acknowledge the Exploration of energization and Radiation in Geospace (ERG) Science Center for providing all-sky imager data. We appreciate Ms. Yuka Yamamoto and Mr. Takumi Adachi of the Technical Center, Nagoya Univ. for their technical assistance on the optical instruments used in this study. SO's contributions to this work has been supported by JSPS KAKENHI 21H04518, 21KK0059, 22H00173, 22K21345, 23K22554, 24H00751, 25H00696, 120263506, 26H02089. DRT's contributions to this study are supported in part through the United Kingdom Natural Environment Research Council (NERC) DRIIVE (NE/W003317/1) and FINESSE (NE/W003147/1) grants. Open Access funding enabled and organized by Projekt DEAL.

References

Astafyeva, E., Yasyukevich, Y. V., Maletckii, B., Oinats, A., Vesnin, A., Yasyukevich, A. S., et al. (2022). Ionospheric disturbances and irregularities during the 25–26 August 2018 geomagnetic storm. *Journal of Geophysical Research: Space Physics*, *127*(1), e2021JA029843. https://doi.org/10.1029/2021JA029843

Berényi, K. A., Barta, V., Szárnya, C., Buzás, A., & Heilig, B. (2025). Subauroral and auroral conditions in the mid- and low-midlatitude ionosphere over Europe during the May 2024 Mother's Day superstorm. *Remote Sensing*, *17*(14), 2492. https://doi.org/10.3390/rs17142492

Borries, C., Jakowski, N., & Wilken, V. (2009). Storm induced large scale TIDs observed in GPS derived TEC. *Annales Geophysicae*, *27*(4), 1605–1612. https://doi.org/10.5194/angeo-27-1605-2009

Caraballo, R., & Bettucci, L. S. (2025). Estimating the 2024 Mother's Day magnetic storm impact on the Uruguayan power grid. *Advances in Space Research*, *77*(4), 5138–5153. https://doi.org/10.1016/j.asr.2025.11.102

Carmo, C. S., Dai, L., Wrasse, C. M., Barros, D., Takahashi, H., Figueiredo, C. A. O. B., et al. (2024). Ionospheric response to the extreme 2024 Mother's Day geomagnetic storm over the Latin American sector. *Space Weather*, *22*(12), e2024SW004054. https://doi.org/10.1029/2024SW004054

Cheng, P.-H., & Morton, Y. J. (2025). Observation of large-scale traveling ionospheric disturbances in the topside ionosphere using POD TEC from multiple LEO satellites constellations. *Journal of Geophysical Research: Space Physics*, *130*(4), e2024JA033293. https://doi.org/10.1029/2024JA033293

De Michelis, P., & Consolini, G. (2025). Unveiling the Gannon storm: How ground-based magnetometers mapped its global impact. *Space Weather*, *23*(6), e2025SW004350. https://doi.org/10.1029/2025SW004350

Ding, F., Wan, W., Liu, L., Afraimovich, E., Voeykov, S., & Perevalova, N. (2008). A statistical study of large-scale traveling ionospheric disturbances observed by GPS TEC during major magnetic storms over the years 2003–2005. *Journal of Geophysical Research*, *113*(A3). https://doi.org/10.1029/2008JA013037

Elvidge, S., & Themens, D. R. (2025). The probability of the May 2024 geomagnetic superstorm. *Space Weather*, *23*(1), e2024SW004113. https://doi.org/10.1029/2024SW004113

Foster, J. C., Erickson, P. J., Nishimura, Y., Zhang, S. R., Bush, D. C., Coster, A. J., et al. (2024). Imaging the May 2024 extreme aurora with ionospheric total electron content. *Geophysical Research Letters*, *51*(20), e2024GL111981. https://doi.org/10.1029/2024GL111981

Garcia, F. J., Taylor, M. J., & Kelley, M. C. (1997). Two-dimensional spectral analysis of mesospheric airglow image data. *Applied Optics*, *36*(29), 7374–7385. https://doi.org/10.1364/AO.36.007374

Grandin, M., Bruus, E., Ledvina, V. E., Partamies, N., Barthelemy, M., Martinis, C., et al. (2024). The Gannon Storm: Citizen science observations during the geomagnetic superstorm of 10 May 2024. *Geoscience Communication*, *7*(4), 297–316. https://doi.org/10.5194/gc-7-297-2024

Inaba, Y., Shiokawa, K., Oyama, S.-I., Otsuka, Y., Connors, M., Schofield, I., et al. (2021). Multi-event analysis of plasma and field variations in source of stable auroral red (SAR) arcs in inner magnetosphere during non-storm-time substorms. *Journal of Geophysical Research: Space Physics*, *126*(4), e2020JA029081. https://doi.org/10.1029/2020JA029081

Jakowski, N., & Hoque, M. M. (2019). Estimation of spatial gradients and temporal variations of the total electron content using ground-based GNSS measurements. *Space Weather*, *17*(2), 339–356. https://doi.org/10.1029/2018SW002119

Ma, G., & Maruyama, T. (2003). Derivation of TEC and estimation of instrumental biases from GEONET in Japan. *Annales Geophysicae*, *21*(10), 2083–2093. https://doi.org/10.5194/angeo-21-2083-2003

Makarevich, R. A., Crowley, G., Azeem, I., Ngwira, C., & Forsythe, V. V. (2021). Auroral E-region as a source region for ionospheric scintillation. *Journal of Geophysical Research: Space Physics*, *126*(5), e2021JA029212. https://doi.org/10.1029/2021JA029212

Meier, R. R., Strickland, D. J., Hecht, J. H., & Christensen, A. B. (1989). Deducing composition and incident electron spectra from ground-based auroral optical measurements: A study of auroral red line processes. *Journal of Geophysical Research*, *94*(A10), 13541–13552. https://doi.org/10.1029/JA094iA10p13541

Mendillo, M., Finan, R., Baumgardner, J., Wroten, J., Martinis, C., & Casillas, M. (2016). A stable auroral red (SAR) arc with multiple emission features. *Journal of Geophysical Research: Space Physics*, *121*(10), 10564–10577. https://doi.org/10.1002/2016JA023258

Mota, E., Camacho, E., & Benyosef, L. (2025). Analysis of the Mother's Day storm effects on equatorial power grids near the equatorial electrojet region. *EGUsphere*, *2025*, 1–25. https://doi.org/10.5194/egusphere-2025-2381

Nishimura, Y., Bruus, E., Karvinen, E., Martinis, C. R., Dyer, A., Kangas, L., et al. (2022). Interaction between proton aurora and stable auroral red arcs unveiled by citizen scientist photographs. *Journal of Geophysical Research: Space Physics*, *127*, e2022JA030570. https://doi.org/10.1029/2022JA030570

Nykiel, G., Cahuasquí, J. A., Hoque, M. M., & Jakowski, N. (2024). Relationship between GIX, SIDX, and ROTI ionospheric indices and GNSS precise positioning results under geomagnetic storms. *GPS Solutions*, *28*(2), 69. https://doi.org/10.1007/s10291-023-01611-5

Nykiel, G., Ferreira, A., Günzkofer, F., Iochem, P., Tasnim, S., & Sato, H. (2024). Large-scale traveling ionospheric disturbances over the European sector during the geomagnetic storm on March 23–24, 2023: Energy deposition in the source regions and the propagation characteristics. *Journal of Geophysical Research: Space Physics*, *129*(3), e2023JA032145. https://doi.org/10.1029/2023JA032145

15427390, 2026, 8, Downloaded from https://agupubs.onlinelibrary.wiley.com/doi/10.1029/2026SW005133 by Dtsch Zentrum F. Luft.U. Raum Fahrt In D. Helmholtz Gemein., Wiley Online Library on [06/10/2026]. See the Terms and Conditions (https://onlinelibrary.wiley.com/terms-and-conditions) on Wiley Online Library for rules of use; OA articles are governed by the applicable Creative Commons License

Ogawa, T., Otsuka, Y., Shiokawa, K., Tsugawa, T., Saito, A., Hoshinoo, K., et al. (2009). Medium-scale traveling ionospheric disturbances and plasma bubbles observed by an all-sky airglow imager at yonaguni, Japan. *Terrestrial, Atmospheric and Oceanic Sciences*, *20*(1), 287–295. https://doi.org/10.3319/TAO.2007.12.06.02(F3C)

Park, J., Spogli, L., Azeez, A., Alfonsi, L., Cesaroni, C., Romano, V., & Akande, A. (2025). The impact of Mother's Day storms in May 2024 on precise point positioning at mid-latitudes. *Annales Geophysicae*, *68*(2), A214. https://doi.org/10.4401/ag-9161

Parker, W. E., & Linares, R. (2024). Satellite drag analysis during the May 2024 Gannon geomagnetic storm. *Journal of Spacecraft and Rockets*, *61*(5), 1412–1416. https://doi.org/10.2514/1.A36164

Paul, K. S., Haralambous, H., Moses, M., Oikonomou, C., Potirakis, S. M., Bergeot, N., & Chevalier, J.-M. (2025). Investigation of the ionospheric response on Mother's Day 2024 geomagnetic superstorm over the European sector. *Atmosphere*, *16*(2), 180. https://doi.org/10.3390/atmos16020180

Pi, X., Mannucci, A. J., Lindqwister, U. J., & Ho, C. M. (1997). Monitoring of global ionospheric irregularities using the worldwide GPS network. *Geophysical Research Letters*, *24*(18), 2283–2286. https://doi.org/10.1029/97GL02273

Prikryl, P., Gillies, R. G., Themens, D. R., Weygand, J. M., Thomas, E. G., & Chakraborty, S. (2022). Multi-instrument observations of polar cap patches and traveling ionospheric disturbances generated by solar wind Alfvén waves coupling to the dayside magnetosphere. *Annales Geophysicae*, *40*(6), 619–639. https://doi.org/10.5194/angeo-40-619-2022

Schaer, S. (1999). *Mapping and predicting the Earth's ionosphere using the global positioning system* (PhD thesis). University of Bern.

Schmölter, E., & Berdermann, J. (2025). The impact of the 2024 Mother's Day storm on aircraft surveillance across Europe. *Space Weather*, *23*(12), e2025SW004718. https://doi.org/10.1029/2025SW004718

Shiokawa, K., Otsuka, Y., Ihara, C., Ogawa, T., & Rich, F. J. (2003). Ground and satellite observations of nighttime medium-scale traveling ionospheric disturbance at midlatitude. *Journal of Geophysical Research*, *108*(A4). https://doi.org/10.1029/2002JA009639

Shiokawa, K., Otsuka, Y., & Ogawa, T. (2009). Propagation characteristics of nighttime mesospheric and thermospheric waves observed by optical mesosphere thermosphere imagers at middle and low latitudes. *Earth Planets and Space*, *61*(4), 479–491. https://doi.org/10.1186/bf03353165

Sobral, J. H. A., Takahashi, H., Abdu, M. A., Muralikrishna, P., Sahai, Y., Zamlutti, C. J., et al. (1993). Determination of the quenching rate of the $O(^1D)$ by $O(^3P)$ from rocket-borne optical (630 nm) and electron density data. *Journal of Geophysical Research*, *98*(A5), 7791–7798. https://doi.org/10.1029/92JA01839

Tang, L., Zhang, H., Li, Y., Xu, F., & Zou, F. (2025). Large-scale traveling ionospheric disturbances over north America and Europe during the May 2024 extreme geomagnetic storm. *IEEE Geoscience and Remote Sensing Letters*, *22*, 1–5. https://doi.org/10.1109/LGRS.2025.3608704

Themens, D. R., Elvidge, S., McCaffrey, A., Jayachandran, P. T., Coster, A., Varney, R. H., et al. (2024). The high latitude ionospheric response to the major May 2024 geomagnetic storm: A synoptic view. *Geophysical Research Letters*, *51*(19), e2024GL111677. https://doi.org/10.1029/2024GL111677

Upadhyay, K., & Pallamraju, D. (2024). First daytime red-line emission measurements of the stable auroral red (SAR) arcs. *Geophysical Research Letters*, *51*(3), e2023GL106292. https://doi.org/10.1029/2023GL106292

Vadas, S. L., Themens, D. R., Huba, J. D., Becker, E., Bossert, K., Goncharenko, L., et al. (2025). Higher-order gravity waves and traveling ionospheric disturbances from the polar vortex jet on 11–15 January 2016: Modeling with HIAMCM-SAMI3 and comparison with observations in the thermosphere and ionosphere. *Journal of Geophysical Research: Space Physics*, *130*(1), e2024JA033040. https://doi.org/10.1029/2024JA033040

Wang, N., Yuan, Y., Li, Z., Montenbruck, O., & Tan, B. (2015). Determination of differential code biases with multi-GNSS observations. *Journal of Geodesy*, *90*(3), 209–228. https://doi.org/10.1007/s00190-015-0867-4

Yang, Z., & Morton, Y. T. J. (2025). Impacts of the May 2024 extreme geomagnetic storm on global high-accuracy GPS positioning solutions. *Space Weather*, *23*(10), e2025SW004547. https://doi.org/10.1029/2025SW004547

Younas, W., Nishimura, Y., Liao, W., Semeter, J. L., Mrak, S., Morton, Y. J., & Groves, K. M. (2025). Spatio-temporal evolution of mid-latitude GPS scintillation and position errors during the May 2024 solar storm. *Journal of Geophysical Research: Space Physics*, *130*(6), e2025JA033839. https://doi.org/10.1029/2025JA033839

15427390, 2026, 8, Downloaded from https://agupubs.onlinelibrary.wiley.com/doi/10.1029/2026SW005133 by Dtsch Zentrum F. Luft-U. Raum Fahrt In D. Helmholtz Gemein., Wiley Online Library on [06/10/2026]. See the Terms and Conditions (https://onlinelibrary.wiley.com/terms-and-conditions) on Wiley Online Library for rules of use; OA articles are governed by the applicable Creative Commons License